# Anisotropic Fano resonance in the Weyl semimetal candidate LaAlSi

Kunyan Zhang ,<sup>1</sup> Tong Wang,<sup>2</sup> Xiaoqi Pang,<sup>2</sup> Fei Han,<sup>3</sup> Shun-Li Shang,<sup>4</sup> Nguyen T. Hung ,<sup>5</sup> Zi-Kui Liu,<sup>4</sup> Mingda Li ,<sup>3</sup>,\* Riichiro Saito,<sup>2</sup>,† and Shengxi Huang ,<sup>1</sup>,‡

<sup>1</sup>Department of Electrical Engineering, The Pennsylvania State University, University Park, Pennsylvania 16802, USA

<sup>2</sup>Department of Physics, Tohoku University, Sendai 980–8578, Japan

<sup>&</sup>lt;sup>3</sup>Department of Nuclear Science and Engineering, Massachusetts Institute of Technology, Cambridge, Massachusetts 02139, USA

<sup>4</sup>Department of Materials Science and Engineering, The Pennsylvania State University, University Park, Pennsylvania 16802, USA

<sup>5</sup>Frontier Research Institute for Interdisciplinary Sciences, Tohoku University, Sendai 980–8578, Japan



(Received 28 September 2020; revised 20 November 2020; accepted 9 December 2020; published 30 December 2020)

Topological Weyl semimetal (WSM) is a solid-state realization of chiral Weyl fermions, whose phonon behaviors provide in-depth knowledge of their electronic properties. In this work, anisotropic Fano resonance is observed in a type-II WSM candidate LaAlSi by polarized Raman spectroscopy. The asymmetric line shape occurs for the  $B_1^2$  phonon mode of LaAlSi only for 488- and 532-nm laser excitations but not for 364-, 633-, and 785-nm excitations, suggesting the excitation selectivity. The asymmetry, frequency, and linewidth of the  $B_1^2$  phonon mode, along with the spectral background, all show fourfold rotational symmetry as a function of the polarization angle in the polarized Raman spectra. While the shift of Raman frequency in a metal or semimetal is typically attributed to Kohn anomaly, here we show that the anisotropic frequency shift in LaAlSi cannot be explained by the effect of Kohn anomaly, but potentially by the anisotropic scattering background of Fano resonance. Origins of the excitation-energy dependence and anisotropic behavior of the Fano resonance are discussed by the first-principles calculated electronic band structure and phonon dispersion.

#### DOI: 10.1103/PhysRevB.102.235162

#### I. INTRODUCTION

Fano resonance describes the asymmetric line shape in optical spectra that originates from the interference between the scattering amplitudes of discrete and continuous states [1]. In the context of Raman spectra, the states involved in Fano resonance correspond to a discrete phonon spectrum and a continuum. When the scattering amplitudes of a phonon and the continuous spectrum are calculated for a given initial state, the Raman intensity is given by taking the modulus square of the total scattering amplitudes, in which the cross term of the scattering amplitudes gives the Fano interference effect. Fano resonance is characterized by an asymmetric Breit-Wigner-Fano (BWF) line shape as [1]

$$I(\omega) = I_0 \frac{[1 + (\omega - \omega_0)/q\Gamma]^2}{1 + [(\omega - \omega_0)/\Gamma]^2}$$
(1)

where  $\Gamma$  and  $\omega_0$  represent, respectively, the linewidth and phonon frequency, and 1/q represents the strength of interference, in which a large |1/q| implies a strong interference. In the limit of  $|1/q| \to 0$ , the spectrum reduces to a Lorentz line shape.

Fano resonance has been reported in a number of artificial structures, including photonic crystals [2,3], nanostructured

plasmonics [4,5], and metamaterials [6], as well as nuclear and solid-state systems. Recently, this phenomenon is reported in the phonon behaviors of topological Weyl semimetals (WSMs) [7,8]. WSM is a quantum material where the energetically low-lying excitations are described by the Weyl equation [9-11]. The bulk Weyl fermions and surface Fermi arcs in WSMs give rise to a plethora of novel phenomena, such as negative magnetoresistance [12-14], nonlocal transport [15], and linear and nonlinear optical phenomena [16-22], that distinguish them from topologically trivial semimetals. An example of WSM is the noncentrosymmetric TaAs family, including TaAs, NbAs, TaP, and NbP. For TaAs, a Fano resonance for the  $A_1$  phonon is observed in the infrared reflectance measurement, in which the Fano resonance arises from the temperature-dependent Weyl-fermion-like excitations [7]. In contrast, the asymmetric Fano resonance of the  $B_1$  Raman-active phonon in NbAs stemmed from phonon self-energy correction is observed to be temperature independent [8]. In TaP, on the other hand, the anisotropy of the  $B_1$ phonon is strongly affected by electron-phonon coupling as a result of nondegenerate energy bands [23].

LaAlSi has a crystal structure similar to the Lorentz-violating type-II WSM LaAlGe, and has been speculated as a promising WSM candidate [24]. Thus, uncovering the optical and electronic properties of LaAlSi is essential to comprehend its potential as a WSM. In this work, we study the polarized Raman spectroscopy of LaAlSi under different excitation laser wavelengths. The observed Raman-active modes show the resonant Raman intensity as a function of the excitation wavelength ranging from near-infrared to ul-

<sup>\*</sup>mingda@mit.edu

<sup>†</sup>rsaito@flex.phys.tohoku.ac.jp

<sup>‡</sup>sjh5899@psu.edu

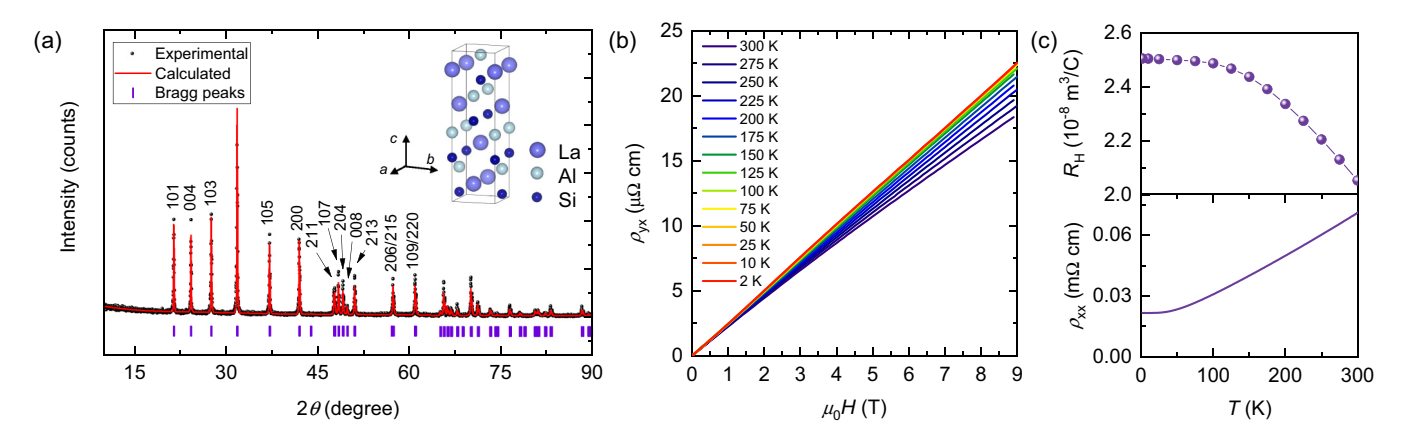


FIG. 1. Crystal structure and Hall measurement of LaAlSi. (a) The powder x-ray diffraction of LaAlSi and the Rietveld refinement. The experimental data can be well fitted with the LaPtGe-type structure. Inset is the crystal structure of LaAlSi. (b) The Hall resistivity  $\rho_{yx}$  as a function of magnetic field at different temperatures. (c) The Hall coefficients  $R_H$  (upper panel) and resistivity  $\rho_{xx}$  (lower panel) as a function of temperature.

traviolet regions. For the  $B_1^2$  mode, we observed the Fano resonance (1/q = -0.1) only for 488- and 532-nm laser excitations. Upon increasing the polarization angle from  $0^{\circ}$  to  $45^{\circ}$ measured from the a crystal axis, the asymmetric Fano line shape reduces to the symmetric Lorentz line shape with minimum intensity. Such anisotropic phonon behavior is unique in solid-state materials. Additionally, the polarization angle dependence of the Fano resonance is accompanied by the changes of Raman frequency and linewidth as a function of the polarization angle. Such anisotropic frequency-shift of the asymmetric phonon mode in LaAlSi cannot be explained by the Kohn anomaly effect, which is generally the reason for phonon softening in a metal as a result of electron-phonon interaction. Instead, the origin of the excitation-energy dependence and anisotropic behavior of the Fano resonance is found to be the angle-dependent scattering background observed at 0–400 cm<sup>-1</sup> which is investigated by first-principles calculations of electronic band structure and phonon dispersion relation. Our work provides valuable insights into the microscopic scattering pathways and transport properties of the WSM candidate LaAlSi, and the methods used can be broadly applied to other quantum materials.

#### II. RESULTS AND DISCUSSION

Single-crystal LaAlSi is synthesized by the flux method. The unit-cell parameters obtained from x-ray diffraction [Fig. 1(a)] are a = 4.3082 Å and c = 14.6617 Å. The magnetic-field dependence of Hall resistivity  $\rho_{vx}$  of LaAlSi shows a linear/sublinear behavior at all temperatures as shown in Fig. 1(b), which indicates a single-band/quasi-single-band domination in the electronic structure, whereas the positive slopes represent the hole-type nature of the dominant carriers. With linear-fittings to the Hall resistivity data, the Hall coefficients  $R_{\rm H}$  at different temperatures can be extracted [Fig. 1(c)]. The carrier density n and carrier mobility  $\mu$  are obtained by  $R_{\rm H}=1/ne$  and  $\rho_{xx}=1/ne\mu$ . Here *n* donates the carrier density, e the electron charge, and  $\mu$  the carrier mobility. The semimetallic nature of LaAlSi is confirmed by the temperature-dependent carrier density obtained from the Hall measurement. The hole-type-carrier density varies

from  $n = 3.04 \times 10^{20} \, \mathrm{cm^{-3}}$  to  $2.49 \times 10^{20} \, \mathrm{cm^{-3}}$  when the measuring temperature decreases from 300 to 2 K (Fig. S1) [25]. The magnitude of the carrier density is two orders smaller than those of conventional metals. For a metal or semimetal, the conductivity decreases with increasing temperature due to enhanced phonon scattering. We observe a monotonic increase of resistivity in LaAlSi with increasing temperature-dependent carrier mobility in Fig. S2 and a previous comparative study on magnetic PrAlSi and nonmagnetic LaAlSi [26].

In the Raman measurement, we adopt a backscattering geometry,  $\bar{Z}(XX)Z$ , in which the incident and scattered lights propagate along the Z and -Z directions (i.e., along the c axis of LaAlSi), respectively, and select the same polarization angles of the incident and scattered beams. LaAlSi has a body-centered tetragonal structure [Fig. 1(a), inset] that belongs to the space group  $I4_1md$  (point group  $C_{4v}$ ). Group theory predicts that LaAlSi has 15 optical phonon modes including degeneracy, whose irreducible representations are  $[2A_1 + 3B_1 + 5E]$ . In the  $\bar{Z}(XX)Z$  geometry, only the  $2A_1$  ( $x^2 + y^2$ ) and  $3B_1$  ( $x^2 - y^2$ ) Raman-active modes are observable, whereas the E modes (xz, yz) are absent.

The Raman spectra for five excitation wavelengths of 364, 488, 532, 633, and 785 nm in the Z(XX)Z geometry are shown in Fig. 2 with the air signals subtracted (Fig. S3), in which the incident and scattered light polarizations are along the a axis of LaAlSi. We observe five peaks at 120, 195, 296, 378, and 422 cm<sup>-1</sup> that are assigned to the  $B_1^1$ ,  $A_1^1$ ,  $B_1^2$ ,  $B_1^3$ , and  $A_1^2$  modes by density-functional theory (DFT) calculations, respectively. The calculated frequencies of the Raman modes are 124.6, 195.8, 303.7, 383.2, and 434.9 cm<sup>-1</sup> (Table S1), which well reproduce the experimental results. The observed Raman intensities of the five peaks distinctly depend on the laser wavelength as shown in Fig. 2(b). For example, the lower-frequency modes,  $B_1^1$  $(120 \text{ cm}^{-1})$  and  $A_1^1$   $(195 \text{ cm}^{-1})$ , have stronger intensities for the longer wavelengths (633 and 785 nm), while they almost disappear for the 364- and 488-nm excitations. On the other hand, the three higher-frequency Raman modes,  $B_1^2$ ,  $B_1^3$ , and  $A_1^2$ , have higher intensities for the 364-, 488-, and

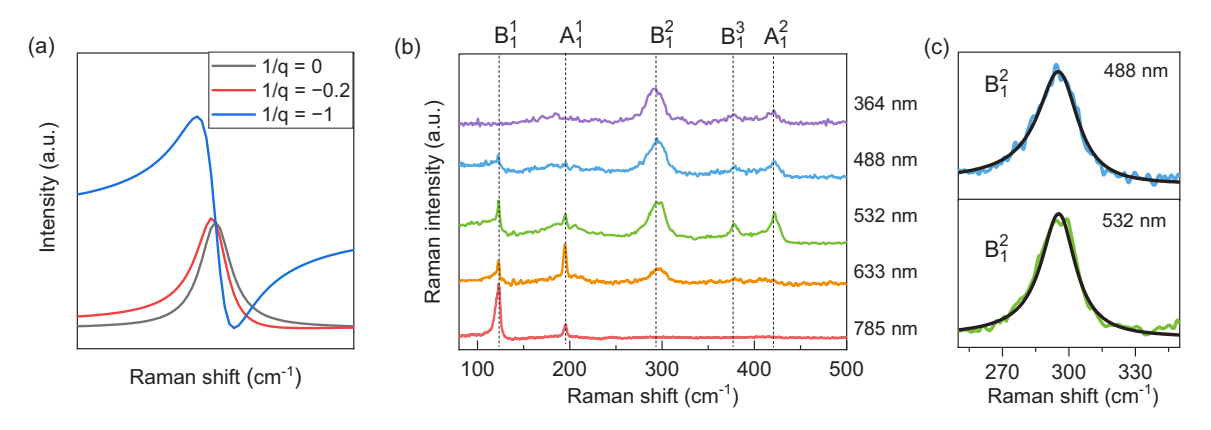


FIG. 2. Raman-active phonon modes of LaAlSi. (a) Illustration of the Lorentz (1/q = 0) and Fano line shapes (1/q = -0.2 and -1). Other parameters in Eq. (1) are taken as  $I_0 = 1$ ,  $\omega_{\text{BWF}} = 0$ ,  $\Gamma = 4$ . (b) Raman spectra for the 364-, 488-, 532-, 633-, and 785-nm excitations. It is noted that the air signals due to high laser power are subtracted from the figure. (c) The enlarged spectra of the  $B_1^2$  mode at 488 nm (top) and 532 nm (bottom) with the BWF fittings (black lines).

532-nm excitations. The excitation-wavelength dependence of Raman intensity suggests that the scattering-resonant effect is phonon-mode dependent, which is analogous to the resonant Raman spectra of the WSM TaP [23]. In the present case of LaAlSi, the 532-nm excitation is unique in the sense that all the Raman peaks are observed with relatively strong intensities.

For the 532- and 488-nm excitations, we observe the anisotropic Fano resonance of the  $B_1^2$  mode at around 296 cm<sup>-1</sup>, which corresponds to the bond stretching motions of Si atoms that are coupled with the rotation of Al atoms in the ab plane. This Raman mode for both wavelengths can be fitted nicely by the BWF function with 1/q = -0.1 (black lines) as shown in Fig. 2(c), which offers a better  $\tilde{\chi}^2$  than the Lorentz functions in our statistical analysis (Fig. S4 and Supplemental Material, Note 1). The observation of BWF line shape suggests that the  $B_1^2$  mode at 296 cm<sup>-1</sup> contributes to the discrete state in the Fano resonance. On the other hand, the continuous spectrum in Fano resonance is typically provided by electronic scattering events known as the electronic Raman scattering (ERS), in which a photoexcited electron excites an electron-hole pair near the Fermi energy by the Coulomb interaction [27-29]. Thus, the appearance of the BWF line shape in Raman spectra is typically evidence that the observed material is a metal or a semimetal. For example, the BWF line shape of the G band at 1580  $\,\mathrm{cm}^{-1}$  is used to distinguish between metallic and semiconducting single-wall carbon nanotubes [27,30] and to evaluate the Fermi energy in graphene [31,32]. However, in the present LaAlSi, another origin of the continuous spectrum, is also expected from the two-phonon scattering, which will be discussed later.

Symmetry assignment of the Raman modes is confirmed by angle-resolved polarized Raman spectroscopy in which LaAlSi crystal is rotated in-plane by the angle  $\theta$  between a axis ( $\theta = 0^{\circ}$ ) and polarization direction. According to Raman tensor theory, Raman intensity of the  $A_1$  mode is isotropic as a function of  $\theta$ , while the intensity of the  $B_1$  mode gives the fourfold symmetry by  $|\cos 2\theta|^2$  for  $\bar{Z}(XX)Z$  geometry. Detailed analysis of the polarization dependence of Raman

intensity using Raman tensor is given in Table S2. In Fig. 3, we show the measured Raman intensity maps for five different laser wavelengths with a polarization-angle interval of 15°. Raman intensity for the  $B_1^1$ ,  $B_1^2$ ,  $B_1^3$  modes show the fourfold symmetry with respect to  $\theta$ , whereas those for the  $A_1^1$  and  $A_1^2$  modes are constant as a function of  $\theta$  for all excitations (see Raman spectra and intensity polar plots in Figs. S5 and S6), consistent with the Raman tensor analysis. DFT calculations of the Raman spectra at different polarization angles reproduce the polarization dependences of the  $B_1$  and  $A_1$  phonon intensities (Fig. S7).

Besides the anisotropic Raman intensity of the  $B_1$  modes, angle-resolved polarized Raman scattering shows another unexpected observation of the Fano resonance. The asymmetry of the  $B_1^2$  mode shows the fourfold rotational symmetry as a function of  $\theta$  (Fig. 4). Similar to the polarization-dependent Raman intensity, the absolute value of 1/q, |1/q| takes a maximum value of 0.1 at  $\theta = 0^{\circ}/90^{\circ}$  for the 532- and 488-nm excitations [Figs. 4(b) and 4(e)]. On the contrary, the value of |1/q| for  $\theta = 45^{\circ}/135^{\circ}$  approaches zero as the Raman spectra become symmetric. Additionally, Raman frequency  $\omega_0$  and linewidth  $\Gamma$  of the  $B_1^2$  mode are also sensitive to the polarization angle  $\theta$  in which the maxima  $\omega_0 = 299 \, \mathrm{cm}^{-1}$  and  $\Gamma = 12 \,\mathrm{cm}^{-1}$  occur at  $\theta = 45^{\circ}/135^{\circ}$  for both the 532- and 488-nm excitations [Figs. 4(c) and 4(f)]. Similarly, for the quantum spin liquid  $\alpha$ -RuCl<sub>3</sub>, Mai et al. also showed that the Fano-shaped  $A_g^2$  mode exhibits modulations of frequency and asymmetry as a function of  $\theta$ , in which the phonon frequency changes by 2.5 cm<sup>-1</sup> between the minimum and the maximum |1/q| at  $\theta = 90^{\circ}$  and  $\theta = 0^{\circ}$  [33]. The origin of such Fano resonance for α-RuCl<sub>3</sub> has been attributed to the continuum originated from the Kitaev magnetic interactions that survive up to room temperature [34,35].

The continuous spectrum from 0 to 400 cm<sup>-1</sup> that contributes to the Fano resonance also exhibits modulations as a function of  $\theta$  only for 532-nm excitation [Fig. 5(a)]. The intensity of the background decreases with increasing  $\theta$  from  $\theta = 0^{\circ}$  to 45° and then increases again from  $\theta = 45^{\circ}$  to 90° for 532 nm as shown by the arrows in Fig. 5(a). Color

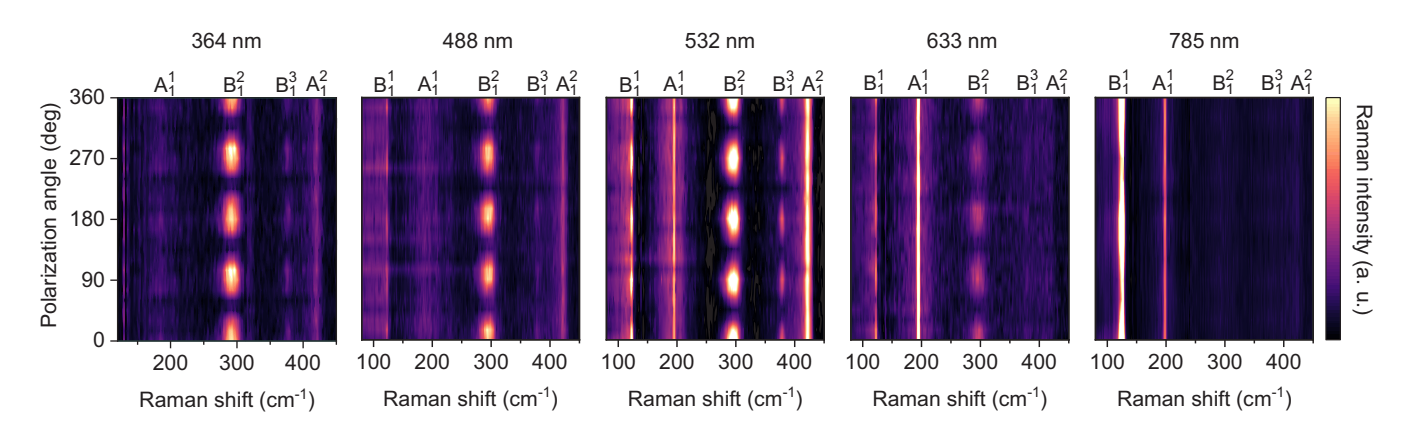


FIG. 3. Color maps of Raman intensity for five excitations. The lower limit of the spectrometer for the 364-nm laser is around 140 cm<sup>-1</sup>. The background spectra and air signals are subtracted from the Raman intensity.

maps of the background fitted using a linear function of the Raman shift in Fig. 5(b) clearly illustrate the fourfold periodicity of the scattering background. In the Fano resonance,  $\frac{\langle \phi|T|i \rangle}{V_k^* \langle \psi_E|T|i \rangle}$ , where  $\langle \phi|T|i \rangle$  is the transition matrix of the modified discrete states and  $\langle \psi_E | T | i \rangle$  is the transition matrix of the continuous states,  $V_E^*$  describes the electron-phonon coupling strength, which gives the linewidth  $\Gamma = \pi |V_E|^2$  [1]. When we rotate  $\theta$  from  $0^{\circ}$  to  $45^{\circ}$ , both |q| and linewidth increase with increasing  $\theta$  (Fig. 4). If the anisotropy of qis solely determined by  $V_E^*$ , they should have been inversely proportional to each other according to the definition of q. This suggests that the anisotropy of either  $\langle \psi_E | T | i \rangle$  or  $\langle \phi | T | i \rangle$  plays a more dominant role than that of  $V_E^*$  in determining the anisotropy of q. Since the amplitude of the scattering background has a similar polarization dependence to that of 1/q, we suspect that the term  $\langle \psi_E | T | i \rangle$  related to the scattering background dominates the observed anisotropy, and that the background has a considerable contribution to the coherent continuous spectrum of the Fano resonance. Similarly, for  $\alpha$ -RuCl<sub>3</sub>, the intensity of the background spectrum increases with increasing |1/q| of the  $A_{\alpha}^2$  mode and disappears with decreasing |1/q|. As mentioned above, the coherent origin of spectral background for graphene can be understood by ERS due to the Coulomb interaction [36,37], whose strength is related to the carrier concentration and thus can be tuned by doping. We expect the ERS in LaAlSi to some extent; however, it is challenging to confirm it by changing the doping concentration in a three-dimensional semimetal. Another possible origin of the spectral background in LaAlSi is the double-resonance Raman scattering of two-phonon emission since phonon dispersion relations of some optical phonon modes show flatband nature from

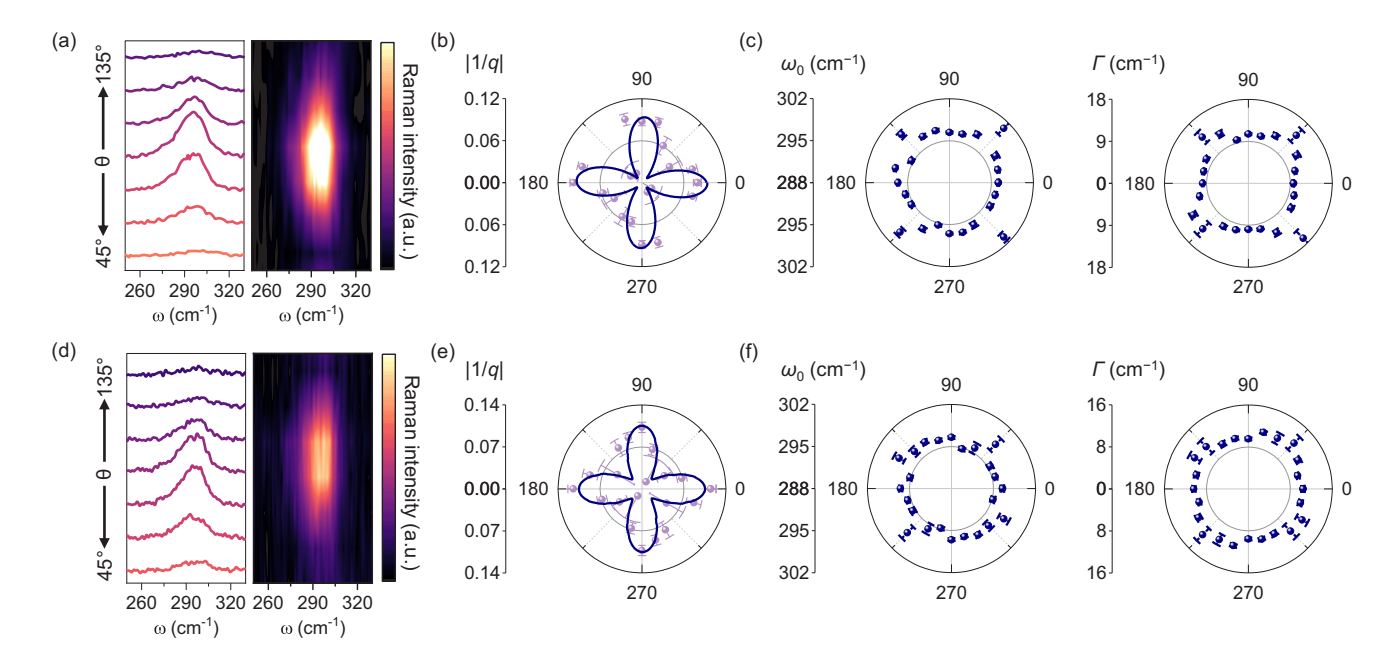


FIG. 4. Fano resonance of LaAlSi. (a) Raman spectra and color maps of the  $B_1^2$  mode from  $\theta = 45^\circ$  to 135° for 532 nm. Background spectra are subtracted using a linear function of the Raman shift for a better view of the mode intensity. (b) |1/q| of the  $B_1^2$  mode for 532 nm. The polar plot is fitted using a sinusoidal function. (c) Polarization dependence of Raman frequency  $\omega_0$  (left) and linewidth  $\Gamma$  (right) of the  $B_1^2$  mode for 532 nm. (d)–(f) The same as (a)–(c) for 488 nm.

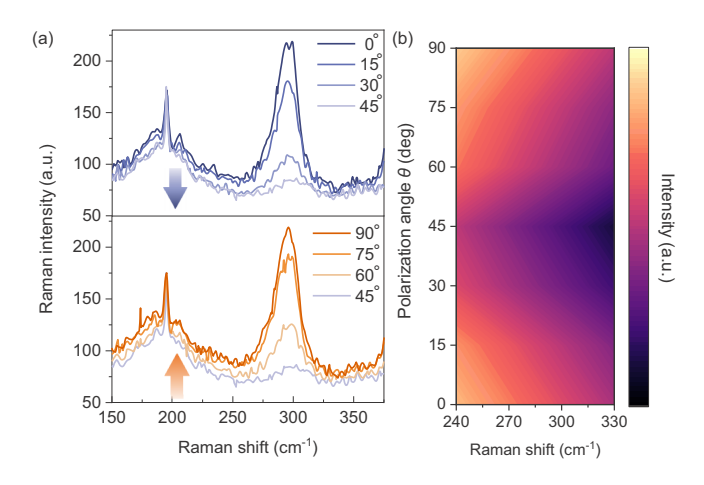


FIG. 5. The continuous spectra for 532-nm excitation. (a) Raman spectra of LaAlSi from  $\theta=0^{\circ}$  to  $90^{\circ}$ . The arrows show the evolution of the scattering background. (b) Polarization dependence of the scattering background.

our first-principles calculations, which will also be discussed later.

To understand the laser- and angle- dependent Raman spectra, we calculate the resonant Raman intensity of LaAlSi based on the DFT calculations. First-order resonant Raman intensity is given by the following formula [38,39]

$$I = \left| \sum_{\boldsymbol{k}, v} \sum_{m, m'} \frac{M_{\text{opt}}^{fm'}(\boldsymbol{k}) M_{\text{ep}, v}^{m'm}(\boldsymbol{k}) M_{\text{opt}}^{mi}(\boldsymbol{k})}{(E_L - E^{mi}(\boldsymbol{k}) - i\gamma)(E_L - E^{m'i}(\boldsymbol{k}) - \hbar\omega_v - i\gamma)} \right|^2,$$

where the summation on the wave vector  $\mathbf{k}$  is taken over the Brillouin zone [Fig. 6(a)], and the labels i, f, m, and m' denote the initial, final, and the two intermediate states of the photoexcited electron, respectively. Here we assume that the final state is the same as the initial state.  $M_{\text{opt}}^{fm'}(\mathbf{k})$  and  $M_{\text{opt}}^{mi}(\mathbf{k})$  are the electron-photon matrix elements and  $M_{\text{ep},\nu}^{m'm}(\mathbf{k})$  is the electron-phonon matrix element, which is calculated by the plane-wave expansion of the wave function [39].  $\omega_{\nu}$  is the phonon frequency of the  $\nu$ th phonon mode at the  $\Gamma$  point in the Brillouin zone.  $E^{mi}(\mathbf{k})$  [or  $E^{m'i}(\mathbf{k})$ ] is the energy difference between the initial state i and the intermediate state m (or m') at  $\mathbf{k}$ .  $E_L$  denotes the energy of the incident light. The

constant broadening factor  $\gamma$  in the resonant Raman process is set to be 0.1 eV in the Raman intensity calculations. The calculated Raman spectra for different excitation wavelengths and polarization angles are shown in Fig. S7.

The unique dependence of Raman intensity on the excitation wavelength can be understood by the calculated electronic band structure and density of states (DOS) of LaAlSi [Fig. 6(b)]. The electronic DOS shows a large peak around 2.3 eV (close to 532 nm) above the Fermi energy with many flat energy bands at the same energy in the left panel. The large DOS in this region provides the unoccupied energy bands for photoexcited electrons to relax to the intermediate states, either by emitting a phonon with wave vector q = 0in the first-order Raman process or by exciting an electronhole pair near the Fermi energy. This enables the resonant scattering process when the electrons at the Fermi level are excited by the 532-nm excitation (green arrows) compared with 488-nm excitation (blue arrows) and other excitation energies, which is the reason why the 532-nm excitation gives relatively large Raman intensity for all phonon modes. This is also consistent with the experimental results that the background spectrum is relatively strong for the 532-nm excitation. Since the optical absorption for 532 nm occurs at particular points in the Brillouin zone, the k value of the photoexcited electrons depends on the polarization direction of the electric field in the xy plane [23,40,41], which is a possible reason for the polarization-dependent background spectrum and the Fano effect.

The calculated phonon dispersion provides another potential origin of the scattering background observed in the measurements other than ERS. In Fig. 6(c), we plot the calculated phonon dispersion (left) and phonon DOS (right) of LaAlSi. The phonon frequencies at the  $\Gamma$  point (q = 0) connect to the first-order Raman modes. In the region between  $100-120~\mathrm{cm}^{-1}$  and  $160-200~\mathrm{cm}^{-1}$  highlighted by red, there are flat phonon dispersion bands related mainly to the rotations of Si  $(200\,\mathrm{cm}^{-1})$  or Al  $(120\,\mathrm{cm}^{-1})$  atoms around the c axis accompanied by the bond-bending vibration (see Supplemental Material, Video 1 and 2, respectively). The reason for the flatband dispersions is that those phonon modes correspond to the rotation of the Si or Al atoms in the unit cell in which only the phase of the rotation changes by changing the wave vector  $\mathbf{q}$ . These flat phonon bands may contribute to the background spectrum since we expect the so-called doubleresonance Raman scattering in which two phonons with  $q \neq$ 

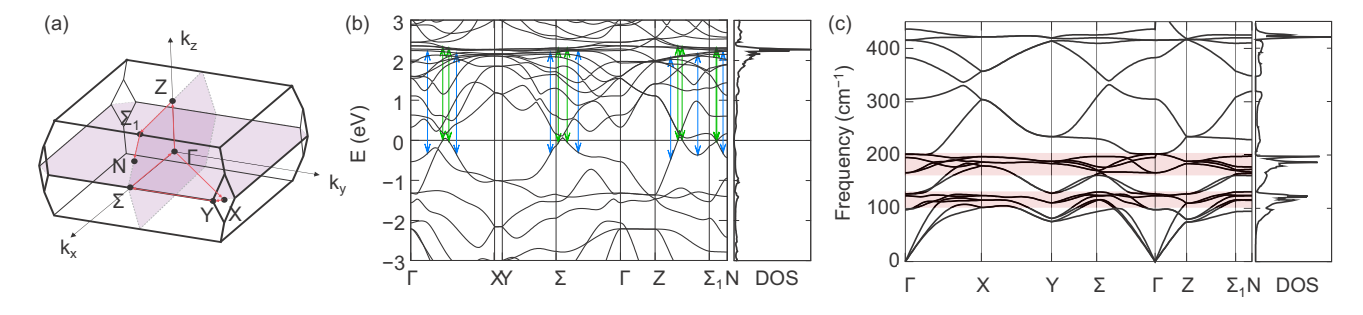


FIG. 6. Electronic band structure and phonon dispersion of LaAlSi. (a) Brillouin zone of LaAlSi. (b) Electronic band structure and density of states of LaAlSi. The green and blue arrows represent the excitation using laser energies of 532- and 488 nm, respectively. (c) Phonon dispersion and density of states of LaAlSi. Flatbands around 100–120 and 160–200 cm<sup>-1</sup> are highlighted.

0 are emitted and a broad spectrum with an energy width up to 400 cm<sup>-1</sup> can arise. It should be pointed out that we cannot precisely pinpoint the origins of the background spectrum to double-resonance Raman scattering or ERS although both origins can be coherent scattering events with the same initial state

Lastly, we comment on the  $\theta$  dependence of the  $B_1^2$  Raman frequency of LaAlSi for the 532-nm excitation, in which the frequency  $\omega_0$  for the  $B_1^2$  mode as a function of  $\theta$  is shifted by 3 cm<sup>-1</sup> from 296 to 299 cm<sup>-1</sup> when the angle increases from 0° to 45°. It is noted that the phonon in LaAlSi can couple to free carriers by electron-phonon interaction, but the electron-phonon interaction known as the Kohn anomaly does not give rise to the angle dependence of phonon frequency. Kohn anomaly is the origin of the frequency modulation of a metal or semimetal, in which the phonon frequency is renormalized by excitation of an electron-hole pair near the Fermi energy by the electron-phonon interaction [42,43]. Since the electronic structure of LaAlSi can potentially host Weyl-nodes-like features near the Fermi energy, the Kohn anomaly effect is possible to occur at phonon wave vector  $q \approx 0$ . However, we rule out the Kohn anomaly effect as the origin of the polarization-dependent Raman frequency, since there is no dependence of light polarization in the phonon softening effect. Thus, further investigation is needed to fully understand the reason for the anisotropic frequency of LaAlSi.

For a phonon mode represented by a symmetric Lorentz function, the mode frequency  $\omega_0$  is the same as the peak frequency at the maximum intensity  $\omega_p$ . This is in sharp contrast with the asymmetric phonon mode described by a BWF function in which the phonon behavior is modified by Fano resonance. The peak frequency  $\omega_p$  is related to the mode frequency  $\omega_0$  as  $\omega_p = \frac{\Gamma}{q} + \omega_0$  derived from  $\frac{dI}{d\omega}|_{\omega_p} = 0$  for  $I(\omega)$  in Eq. (1). If the 1/q is negative as in the present case, the frequency of the maximum intensity  $\omega_p$   $(1/q \neq 0)$  will be on the lower side than that of the symmetric mode  $\omega_p = \omega_0(1/q = 0)$  as shown in Fig. 2(a). Similarly, the peak frequency  $\omega_p$  can also be adjusted by the change of mode linewidth  $\Gamma$ .

## III. CONCLUSIONS

The present work investigates the angle-resolved polarized Raman spectra of a WSM candidate LaAlSi for multiple excitation wavelengths ranging from near-infrared to ultraviolet region. The Raman-active modes show a unique excitation wavelength dependence, as well as anisotropic Raman intensity and frequency as functions of the polarization angle. In particular, we have observed a Fano line shape in the  $B_1^2$  mode for two excitation wavelengths, 488 and 532 nm, which is interpreted as a result of Fano resonance between the  $B_1^2$  phonon and the scattering background. By fitting the asymmetric Raman spectra using the BWF line shape, we found that the asymmetric parameter |1/q| of the  $B_1^2$  phonon mode also shows fourfold rotational dependence on the polarization angle. In order to understand these phenomena, we have calculated resonant Raman intensity by DFT-based first-principles calculations. The origin of the excitation wavelength dependence of the Raman spectra is attributed to the high electron DOS at 2.3 eV above the Fermi level in the

electronic band structure. Though the frequency shift of the  $B_1^2$  mode cannot be explained by the Kohn anomaly effect, it possibly stems from the background spectrum that shares the same polarization dependence with |1/q|. Both ERS and double-resonance Raman scattering due to the flat phonon bands, as shown by the calculated phonon dispersion, can contribute to the formation of the background spectrum. This study features the unconventional Raman anisotropy of the topological semimetal candidate LaAlSi, which sheds light on understanding the elementary excitation of phonon behaviors in metallic and semimetallic materials.

#### IV. EXPERIMENTAL SECTION

#### A. Crystal synthesis

LaAlSi crystals used in this research were grown via the flux method. Approximately 5 grams of lanthanum ingots (>= 99.9%, Alfa Aesar), aluminum beads (>= 99.9%, Sigma-Aldrich), and silicon powders (>= 99.995%, Beantown Chemical) in the mole ratio of 1:10:1 were weighed, mixed, and placed in a 5-mL alumina crucible. All handling was performed in a glove box with a protective argon atmosphere (both H<sub>2</sub>O and O<sub>2</sub> are limited below 0.1 ppm). Then the alumina crucible containing the starting materials was flame sealed in an evacuated quartz ampule. The ampule was heated to 1000 °C in a box furnace and kept at the temperature for 10 h. Subsequently, a slow-cooling process at the rate of 5 °C/h was carried out from 1000 to 500 °C, and at 500 °C the excess aluminum flux was removed by centrifugation. The obtained crystals are shiny plates with metallic luster and have a typical dimension of  $5 \times 5 \times 0.5 \text{ mm}^3$ .

### B. Resistivity and Hall effect

Transport measurements including resistivity and Hall effect were performed on the Quantum Design Physical Property Measurement System. Resistivity and Hall effect measurements were simultaneously carried out on a rectangle crystal using a five-probe geometry [42,43]. The current is along the a or b axes (a and b are equivalent) and the magnetic fields were applied along the c axis.

### C. Raman spectroscopy

Raman spectroscopy measurements were performed on a Horiba LabRAM HR Evolution Raman spectrometer. The Raman measurements were performed at room temperature. Incident lasers with wavelengths of 364, 488, 532, 633, and 785 nm were focused on the sample using a 50× objective. An 1800-grooves/mm grating and a linear polarization analyzer were coupled to the spectrometer to collect the scattered light. Laser power was maintained at around 5 mW to ensure an ideal signal to noise ratio.

#### D. DFT calculations

Home-made programs of first-principles calculations were used to calculate the electron-photon and electron-phonon interactions to obtain the Raman tensor and Raman intensity in Eq. (2), respectively [39]. The DFT calculations for electronic and phonon energy dispersions were performed by the

QUANTUMESPRESSO package [44]. The ground state of LaAlSi is calculated by the norm-conserving pseudopotential with local-density approximation [45] and the cutoff energy is set to be 180 Ry to achieve the convergence of total energy. The Monkhorst-Pack k mesh is set to  $6 \times 6 \times 6$  and  $10 \times 10 \times 10$  for the self-consistent and non-self-consistent field calculations, respectively. In these calculations, the LaAlSi structure was optimized to be a = b = 4.24 Å, and c = 15.14 Å. Then we obtained the electron-photon matrix combined with the home-made program [39]. And, with using the electron-phonon Wannier (EPW) package [46], the electron-phonon matrix for (q = 0) phonon was obtained. Note that only phonon at  $\Gamma$  point (q = 0) was considered for the first-order Raman process in this study.

#### ACKNOWLEDGMENTS

K.Z. acknowledges the support from Milton and Albertha Langdon Memorial Graduate Fellowship. T.W. acknowledges the MEXT scholarship, Japan. X.P. and T.W. acknowledge the GP-MS programs, Tohoku University. F.H. and M.L. acknowledge the support from US DOE BES Award No. DE-SC0020148. S.L.S. and Z.K.L. acknowledge the financial support from the U. S. National Science Foundation Grant No. CMMI-1825538. N.T.H. acknowledges JSPS KAKENHI Grant No. JP20K15178. R.S. acknowledges JSPS KAKENHI Grant No. JP18H01810. S.H. acknowledges the support from the U. S. National Science Foundation Grant No. ECCS-1943895.

- [1] U. Fano, Phys. Rev. 124, 1866 (1961).
- [2] M. F. Limonov, M. V. Rybin, A. N. Poddubny, and Y. S. Kivshar, Nat. Photonics 11, 543 (2017).
- [3] W. Zhou, D. Zhao, Y.-C. Shuai, H. Yang, S. Chuwongin, A. Chadha, J.-H. Seo, K. X. Wang, V. Liu, Z. Ma, and S. Fan, Prog. Quantum Electron. 38, 1 (2014).
- [4] A. E. Miroshnichenko, S. Flach, and Y. S. Kivshar, Rev. Mod. Phys. 82, 2257 (2010).
- [5] M. Rahmani, B. Luk'yanchuk, and M. Hong, Laser Photonics Rev. 7, 329 (2013).
- [6] B. Luk'yanchuk, N. I. Zheludev, S. A. Maier, N. J. Halas, P. Nordlander, H. Giessen, and C. T. Chong, Nat. Mater. 9, 707 (2010).
- [7] B. Xu, Y. M. Dai, L. X. Zhao, K. Wang, R. Yang, W. Zhang, J. Y. Liu, H. Xiao, G. F. Chen, S. A. Trugman, J. X. Zhu, A. J. Taylor, D. A. Yarotski, R. P. Prasankumar, and X. G. Qiu, Nat. Commun. 8, 14933 (2017).
- [8] J. Coulter, G. B. Osterhoudt, C. A. C. Garcia, Y. Wang, V. M. Plisson, B. Shen, N. Ni, K. S. Burch, and P. Narang, Phys. Rev. B 100, 220301(R) (2019).
- [9] B. Q. Lv, H. M. Weng, B. B. Fu, X. P. Wang, H. Miao, J. Ma, P. Richard, X. C. Huang, L. X. Zhao, G. F. Chen, Z. Fang, X. Dai, T. Qian, and H. Ding, Phys. Rev. X 5, 031013 (2015).
- [10] S.-Y. Xu, I. Belopolski, N. Alidoust, M. Neupane, G. Bian, C. Zhang, R. Sankar, G. Chang, Z. Yuan, C.-C. Lee, S.-M. Huang, H. Zheng, J. Ma, D. S. Sanchez, B. Wang, A. Bansil, F. Chou, P. P. Shibayev, H. Lin, S. Jia, and M. Z. Hasan, Science 349, 613 (2015).
- [11] H. Weng, C. Fang, Z. Fang, B. A. Bernevig, and X. Dai, Phys. Rev. X 5, 011029 (2015).
- [12] X. Huang, L. Zhao, Y. Long, P. Wang, D. Chen, Z. Yang, H. Liang, M. Xue, H. Weng, Z. Fang, X. Dai, and G. Chen, Phys. Rev. X 5, 031023 (2015).
- [13] D. T. Son and B. Z. Spivak, Phys. Rev. B 88, 104412 (2013).
- [14] F. Arnold, C. Shekhar, S.-C. Wu, Y. Sun, R. D. dos Reis, N. Kumar, M. Naumann, M. O. Ajeesh, M. Schmidt, A. G. Grushin, J. H. Bardarson, M. Baenitz, D. Sokolov, H. Borrmann, M. Nicklas, C. Felser, E. Hassinger, and B. Yan, Nat. Commun. 7, 11615 (2016).
- [15] S. A. Parameswaran, T. Grover, D. A. Abanin, D. A. Pesin, and A. Vishwanath, Phys. Rev. X 4, 031035 (2014).

- [16] S. Patankar, L. Wu, B. Lu, M. Rai, J. D. Tran, T. Morimoto, D. E. Parker, A. G. Grushin, N. L. Nair, J. G. Analytis, J. E. Moore, J. Orenstein, and D. H. Torchinsky, Phys. Rev. B 98, 165113 (2018).
- [17] D. Neubauer, A. Yaresko, W. Li, A. Löhle, R. Hübner, M. B. Schilling, C. Shekhar, C. Felser, M. Dressel, and A. V. Pronin, Phys. Rev. B 98, 195203 (2018).
- [18] S.-i. Kimura, H. Yokoyama, H. Watanabe, J. Sichelschmidt, V. Süß, M. Schmidt, and C. Felser, Phys. Rev. B 96, 075119 (2017).
- [19] L. Wu, S. Patankar, T. Morimoto, N. L. Nair, E. Thewalt, A. Little, J. G. Analytis, J. E. Moore, and J. Orenstein, Nat. Phys. 13, 350 (2017).
- [20] B. Xu, Y. M. Dai, L. X. Zhao, K. Wang, R. Yang, W. Zhang, J. Y. Liu, H. Xiao, G. F. Chen, A. J. Taylor, D. A. Yarotski, R. P. Prasankumar, and X. G. Qiu, Phys. Rev. B 93, 121110(R) (2016).
- [21] G. B. Osterhoudt, L. K. Diebel, M. J. Gray, X. Yang, J. Stanco, X. Huang, B. Shen, N. Ni, P. J. W. Moll, Y. Ran, and K. S. Burch, Nat. Mater. 18, 471 (2019).
- [22] Q. Ma, S.-Y. Xu, C.-K. Chan, C.-L. Zhang, G. Chang, Y. Lin, W. Xie, T. Palacios, H. Lin, S. Jia, P. A. Lee, P. Jarillo-Herrero, and N. Gedik, Nat. Phys. 13, 842 (2017).
- [23] K. Zhang, X. Pang, T. Wang, F. Han, S.-L. Shang, N. T. Hung, A. R. T. Nugraha, Z.-K. Liu, M. Li, R. Saito, and S. Huang, Phys. Rev. B 101, 014308 (2020).
- [24] S.-Y. Xu, N. Alidoust, G. Chang, H. Lu, B. Singh, I. Belopolski, D. S. Sanchez, X. Zhang, G. Bian, H. Zheng, M.-A. Husanu, Y. Bian, S.-M. Huang, C.-H. Hsu, T.-R. Chang, H.-T. Jeng, A. Bansil, T. Neupert, V. N. Strocov, H. Lin, S. Jia, and M. Z. Hasan, Sci. Adv. 3, e1603266 (2017).
- [25] See Supplemental Material at http://link.aps.org/supplemental/ 10.1103/PhysRevB.102.235162 for transport measurement, polarized Raman spectra measurement, and analysis.
- [26] M. Lyu, J. Xiang, Z. Mi, H. Zhao, Z. Wang, E. Liu, G. Chen, Z. Ren, G. Li, and P. Sun, Phys. Rev. B 102, 085143 (2020).
- [27] E. H. Hasdeo, A. R. T. Nugraha, K. Sato, M. S. Dresselhaus, and R. Saito, Phys. Rev. B 88, 115107 (2013).
- [28] H. Farhat, S. Berciaud, M. Kalbac, R. Saito, T. F. Heinz, M. S. Dresselhaus, and J. Kong, Phys. Rev. Lett. 107, 157401 (2011).
- [29] D. Zhang, J. Yang, M. Li, and Y. Li, ACS Nano 10, 10789 (2016).

- [30] S. D. M. Brown, A. Jorio, P. Corio, M. S. Dresselhaus, G. Dresselhaus, R. Saito, and K. Kneipp, Phys. Rev. B 63, 155414 (2001).
- [31] E. H. Hasdeo, A. R. T. Nugraha, M. S. Dresselhaus, and R. Saito, Phys. Rev. B 90, 245140 (2014).
- [32] D. Yoon, D. Jeong, H.-J. Lee, R. Saito, Y.-W. Son, H. C. Lee, and H. Cheong, Carbon 61, 373 (2013).
- [33] T. T. Mai, A. McCreary, P. Lampen-Kelley, N. Butch, J. R. Simpson, J.-Q. Yan, S. E. Nagler, D. Mandrus, A. R. Hight Walker, and R. V. Aguilar, Phys. Rev. B 100, 134419 (2019).
- [34] J. Knolle, G.-W. Chern, D. L. Kovrizhin, R. Moessner, and N. B. Perkins, Phys. Rev. Lett. 113, 187201 (2014).
- [35] B. Perreault, J. Knolle, N. B. Perkins, and F. J. Burnell, Phys. Rev. B 92, 094439 (2015).
- [36] K. F. McCarty, J. Z. Liu, R. N. Shelton, and H. B. Radousky, Phys. Rev. B 42, 9973 (1990).
- [37] J. W. Quilty, S. Lee, A. Yamamoto, and S. Tajima, Phys. Rev. Lett. **88**, 087001 (2002).
- [38] M. S. Dresselhaus, G. Dresselhaus, R. Saito, and A. Jorio, Phys. Rep. 409, 47 (2005).
- [39] Y. Tatsumi and R. Saito, Phys. Rev. B 97, 115407 (2018).
- [40] X. Ling, S. Huang, E. H. Hasdeo, L. Liang, W. M. Parkin, Y. Tatsumi, A. R. T. Nugraha, A. A. Puretzky, P. M. Das, B. G.

- Sumpter, D. B. Geohegan, J. Kong, R. Saito, M. Drndic, V. Meunier, and M. S. Dresselhaus, Nano Lett. **16**, 2260 (2016).
- [41] S. Huang, Y. Tatsumi, X. Ling, H. Guo, Z. Wang, G. Watson, A. A. Puretzky, D. B. Geohegan, J. Kong, J. Li, T. Yang, R. Saito, and M. S. Dresselhaus, ACS Nano 10, 8964 (2016).
- [42] W. Kohn, Phys. Rev. Lett. 2, 393 (1959).
- [43] T. Nguyen, F. Han, N. Andrejevic, R. Pablo-Pedro, A. Apte, Y. Tsurimaki, Z. Ding, K. Zhang, A. Alatas, E. E. Alp, S. Chi, J. Fernandez-Baca, M. Matsuda, D. A. Tennant, Y. Zhao, Z. Xu, J. W. Lynn, S. Huang, and M. Li, Phys. Rev. Lett. 124, 236401 (2020).
- [44] P. Giannozzi, S. Baroni, N. Bonini, M. Calandra, R. Car, C. Cavazzoni, D. Ceresoli, G. L. Chiarotti, M. Cococcioni, I. Dabo, A. Dal Corso, S. de Gironcoli, S. Fabris, G. Fratesi, R. Gebauer, U. Gerstmann, C. Gougoussis, A. Kokalj, M. Lazzeri, L. Martin-Samos, N. Marzari, F. Mauri, R. Mazzarello, S. Paolini, A. Pasquarello, L. Paulatto, C. Sbraccia, S. Scandolo, G. Sclauzero, A. P. Seitsonen, A. Smogunov, P. Umari, and R. M. Wentzcovitch, J. Phys.: Condens. Matter 21, 395502 (2009).
- [45] J. P. Perdew and A. Zunger, Phys. Rev. B 23, 5048 (1981).
- [46] A. A. Mostofi, J. R. Yates, Y.-S. Lee, I. Souza, D. Vanderbilt, and N. Marzari, Comput. Phys. Commun. 178, 685 (2008).